

# Effect of Y/Mg Ion Ratio and Phase Assemble on Ionic Conductivity of ZrO<sub>2</sub> Solid Electrolyte Ceramics

Y.G. Hoo (✉ [hygdyt2002@126.com](mailto:hygdyt2002@126.com))

Huazhong University of Science and Technology <https://orcid.org/0000-0002-3665-5485>

Jianzhong Xiao

Huazhong University of Science and Technology

Feng Xia

Huazhong University of Science and Technology

---

## Research Article

**Keywords:** phase assemble, zirconia electrolyte, ionic conductivity, SOFCs

**Posted Date:** June 30th, 2020

**DOI:** <https://doi.org/10.21203/rs.3.rs-37162/v1>

**License:**   This work is licensed under a Creative Commons Attribution 4.0 International License.

[Read Full License](#)

---

# Abstract

The phase composition design principle is introduced to obtain a balanced properties of ionic conductivity and thermo-tolerant for zirconia solid electrolyte used in solid oxide fuel cells (SOFCs). The zirconia ceramic solid electrolytes were fabricated by two-step sintering. With increasing Y/Mg ionic ratio from 1.78:1 to 1.88:1, the content of monoclinic phase was not fluctuated widely. The ionic conductivity, including the total electrical resistance; grain electrical resistance and grain boundary electrical resistance at 1223K, was gradually declining with increasing of Y/Mg ionic ratio. Furthermore, the enrichment of Mg ion in grain boundary acts as a disincentive to grain boundary ionic conductivity. In addition, the maximum ionic conductivity at high temperature in this study reaches to  $0.143 \text{ Scm}^{-1}$  with increase of the Y/Mg ion ratio.

## 1. Introduction

The “first generation” solid oxide fuel cells (YSZ-based) possess potential high-performance [1-3] but high operating temperature about  $900^{\circ}\text{C}$  for using hydrogen fuel. As a clean energy, the emission is only water. However, the high grain boundary resistance for oxygen ion transport and weak refractory [4, 5] of YSZ-based solid electrolyte constrained its industrial application. The rare-earth elements doped electrolytes offer potential exceptional performance at lower temperature [6-8], but the high costs and rough running performance results in materials continuous service challenges.

As lower-costs raw materials, magnesia doping ultrathin electrolytes demonstrated good thermal shock resistance [9-10]. Magnesia and yttria complex doping with sintering agents such as Al and Ca oxide also offer other benefits compared to rare-earth elements doping electrolytes, which include lower sintering temperature and compatibility two types conduction. However, Y/Mg complex doping solid electrolytes performance is not intriguing and lagging behind YSZ. In recent years, core-shell structured electrolytes possessing attractive conductivity performance have been suggested by our theoretical derivation to reach the potential superiority of the complex doping solid electrolytes which also behave excellent combination properties. We know, with the increasing of magnesia element, the sintering temperature reaches to  $1750^{\circ}\text{C}$  even over  $1800^{\circ}\text{C}$  for several tens hours. The higher temperature of sintering and the longer time for holding, the more expansive it costs. Therefore, a clear understanding of sintering mechanisms plays a key role in fabricating the high performance zirconia solid electrolytes inexpensively.

In the present work, the complex  $\text{Y}_2\text{O}_3/\text{MgO}/\text{Al}_2\text{O}_3/\text{CaO}$  doped zirconia solid electrolytes were fabricated by two-step pressureless sintering method. For the first time, we reports a densification model with six sub-stages for partially stability zirconia and suggests a kinetic function of densification in the initial sintering stage. Then we investigated the microstructure characteristic and ionic electrical conductivity by adjusting Y/Mg ion ratio. The influence of Y/Mg ion ratio on the microstructure, phase characteristic was also studied and the conduction mechanism was discussed in detail.

## 2. Experimental Processes

The raw powders was supplied by Sansai Company (Yixing, China). The complex doped zirconia raw materials were designed as shown in Table 1. The particle size distribution is determined by a SA-CP3 type particle size analyzer (Japan) with bimodal distribution of 1 $\mu$ m and 4.5 $\mu$ m. The process of Zr-Y-Mg-Al-Ca-O specimen preparation includes the following four steps, as shown in Fig.1: (i) milling of powder with 10vol%-PVA aqueous suspension (powder-to-ball weight ratio of 5:1, with a rotation speed of 150 rpm for 5h); (ii) filtering of powder so as to exclude the powder above 10 $\mu$ m; (iii) filling the dried undersize powders (d50 is 1-5 $\mu$ m) to be pressed by isostatic forming machine at 80 MPa forming targeted sample which shows three advantages when compared to other traditional technologies such as injection molding: (1) no special process of binding exclusion, (2) high density, work simplification and cost-effective, (3) adequate evenly distributed powder with no particle settlement; (iv) sintering of the formed samples by two-step sintering in air atmosphere with a 3°C/min heat-up rate. For seeking a better densification mechanisms, The green bodies (SP1 is Y<sub>2</sub>O<sub>3</sub>-ZrO<sub>2</sub>: MgO-ZrO<sub>2</sub>: CaO-ZrO<sub>2</sub>: Al<sub>2</sub>O<sub>3</sub>-ZrO<sub>2</sub>= 60:18:15:7 (wt %), SP2 is the same proportion but uncoated with PVA solution as a contrast) were then sintered with online imaging Instrument (SJY-2, Xiangtan, China) in Ar atmosphere with a 10°C/min heat-up rate to 1650°C. And the photographs were captured every 100°C before 1200°C, every 20°C before 1500°C, and every 15°C after 1500°C during sintering, respectively. The exact in-situ measurement of the dimensional change was obtained by Image-Pro software with an accuracy of 2  $\mu$ m. Based on these data, the shrinkage values in x, y directions varied with temperature were determined. The terminal density of specimen after sintering was obtained by Archimedes principle. The surface microstructures and fracture diagrams of SP1 and SP2 specimens were observed by scanning electron microscope (Quanta 200, FEI).

**Table 1:** Compositions of raw materials (/mol%)

Sample	ZrO <sub>2</sub>	Y <sub>2</sub> O <sub>3</sub>	MgO	CaO	Al <sub>2</sub> O <sub>3</sub>
S1	89.96	4.58	2.56	2	1
S2	89.96	4.62	2.52	2	1
S3	89.96	4.66	2.48	2	1

Finally, the ionic conductivity of specimen coated with Pt (6mm × 6mm × 1mm) were measured every 100°C for holding 5min from 450°C to 1000°C by Frequency Response Analyzer (Solartron 1260, UK) in the frequency range of 0.01Hz-10MHz. The activation energy is calculated by the conductivity obtained from different temperature. Phase characteristics were presented by X`Pert PRO diffraction (PANalytical B.V., Cu-Ka) at a scan rate of 0.2°/min (parameters: electric voltage = 40kV, electric current = 20mA, scan range 2 $\theta$ =20-90°). The monoclinic phase content is calculated by the formula shown in (1) [11]. The

surface microstructure of electrolytes specimens were observed by scanning electron microscope (Quanta 200, FEI).

$$V_m(\%) = \frac{I_m(111)+I_m(11\bar{1})}{I_m(111)+I_m(11\bar{1})+I_{t+c}(111)} \times 100\% \quad (1)$$

## 3. Results And Discussion

### 3.1 Densification mechanisms

Fig.2 (a) and (b) show the densification tendency in x and y directions of SP1 and SP2 when sintering. It can be seen from the results shown in Fig. 2(a), with increasing of temperature, there shows a linear densification in x direction before 1200°C and a sharp increasing of densification rate after 1200°C. A platform is occurring around 1500°C, which indicated the pausing of densification. With the temperature increasing to 1625°C, the sintering end-point, the shrinkage value declines to zero again. There also illustrates linear densification in y direction before 1200°C and shows a sharp increasing of densification rate after 1200°C. However, the densification rate is higher than that in x direction before 1400°C, and the untimely densification in y direction is occurring comparison with that in x direction. From Fig. 2b, it shows that the densification of unprocessed SP2 is very different with that of SP1. The densification rate in y direction is smaller than that of x direction before 1250°C. The platform, indicated the stopping of densification, is occurring

at 1500°C later than that of SP1; and the final point of sintering in x direction is not observed before 1650°C. According to sintering theory, a densification platform indicates a neck forming or mass transport at grain boundary, which needs more Gibbs energy as sintering force.

From results of the main sintering curve (shown in Fig. 2), the densification rate change associated with unequal distance among particles will be described as three stages-initial, intermediate and final. The porous phase is removed slowly with the increasing of temperature before 1200°C; the densification or the arrangement of particles is occurring in the range of 1200-1500°C. In this stage, the solid particles are connected and the pores are filled through mass transport. After 1500°C, the densification rate falls off gradually until stopping again. Volume diffusion accompanied with an elastic flow but plastic deformation (called high temperature creep deformation) in the final stage of sintering.

We suggested the densification mechanisms to be divided into two types: 1) the chemical potential induced; 2) the spatial force induced. But it can be divided to six sub-stages, to characterize the sintering period. The six sub-stages, to describe the densification, are presented in Fig.3. In the first initial sub-stage (I-1), with the PVA coating in SP1, the elastic flow of PVA increases the densification rate in y direction until the volatile component burnt. After the organic combusted, the second initial sub-stage (I-2), the slower densification rate in x direction, as a gas emission passage, is beneficial to further densification in

y direction. With the gas discharging, the pore adjacent to grains slowly closed. In first intermediate sub-stage (II-1), because of the high activation energy of processed powders by mechanical method, the surface energy decreases with the particle rearrangement or particle restoration through bonding the tiny powder to the small one. The pores located near the tiny powders closed while the bonding continues in the second intermediate sub-stage (II-2), and the further particle rearrangement was continued. The most significant change in intermediate stage is the secondary powder combined with others. The densification rate in this stage is great higher than that in initial stage, but the total shrinkages are similar to that in initial stage. The occurring of first shrinkage platform was the start of final stage. During the final sub-stage (III-1), the grain boundary migration and coalescence continues when the separate pores consumed. The bonded grains were becoming one grain with the disappearance of grain boundary which causes the densification rate near to zero. This phenomenon indicated that the densification is nearly completed according to conventional sintering theory. Differently, in this study, the further densification following the sintering platform takes place in the final sub-stage (III-2) and the mass transport in particle is considered as a global concept. According to traditional sintering theory, the grain boundary will be straight in the final stage of sintering, which cannot give a clear interpretation for partially stability zirconia polycrystalline ceramics. In this study, the spatial force balance is a key factor to affect the final densification of ceramics, especially for the polycrystalline material.

### **3.2 Elements distribution, microstructure and phase assemblage**

Fig.4 implicates the Y and Mg element distribution in sintered S1 sample. The Y ion is clearly visible in the area of grains (shown in Fig.4c), and it can be seen that the Mg ion is mostly distributed along the grain boundaries (shown in Fig.4a). Furthermore, the accumulative Mg ion is obviously seen in Fig.4a owing to the forming of Mg-Al spinel. With the aim of studying the influence of additive ion ratio on phase assemblage of Zr-Y-Mg-Al-Ca-O ceramic, XRD is conducted on the samples with different Y/Mg ion rate. The XRD patterns and microstructure are illustrated in Fig. 5, respectively. As shown in Figure 5d, it can be seen that the fractions of m phase in the three samples, which are mainly similar, do not correlate with the increasing of Y/Mg ion ratio. Moreover, the number of coarse grains shown in SEM pictures is varied with the content of addition. With the increase of Y ion, the number of coarse grains drops gradually. But there are some sub-coarse grains with the increasing of Y/Mg ion ratio. This could be associated with the block effect of spinel [12]. With the increasing of Mg ion content, the black spinel grains are conspicuous. According to our previous studying [13], the coarsening grains were related to heat treat process. But in this study, a same sintering process has been conducted on all samples; therefore, from Fig.5, it can be concluded that there has a more important influence on grain size rather than the m phase content with the increasing of Y/Mg ion ratio if sintered by a similar sintering process.

### **3.3 Ionic conductivity and conduction mechanism**

The ionic conductivities of the sintered samples were studied by Frequency Response Analyzer in temperature range from 723K to 1273K. As for the Zr-Y-Mg-Al-Ca-O ceramic, the typical impedance spectra is consisted with a high-frequency impedance arc and a low-frequency impedance arc related to

the grain and grain boundary resistor-capacitor (RC) effect, respectively (shown in Fig.6). From the impedance spectra shown in Fig.6, it can be seen that with increase of Y/Mg ion ratio, there are all gradually declining in the total electrical resistance, grain electrical resistance and grain boundary electrical resistance tested at 1223K. The declined rate in grain electrical resistance is diminishing. But it is proportionate drop in grain boundary electrical resistance at that temperature with the increasing of Y/Mg ion ratio. Based on the element distribution, as shown in Fig.4, the decreasing grain boundary electrical resistance is related to the decreasing of Mg ion content along grain boundary. On the other hand, the enrichment of Mg ion in grain boundary acts as a disincentive to grain boundary ionic conductivity. Furthermore, the grain ionic conductivity increasing effect by the increasing of Y ion content is weakened slowly as the saturated substitutional effect of Y ion for Zr ion lattice site.

As the result of ionic conductivity shown in Fig.7, calculated by Arrhenius function, it reveals that the ionic conductivity of S3 is the highest at high temperature which is in accordance with impedance spectra. However, a random arrangement of that over lower temperature windows is found, which may be related to the influence extent of grain boundary electrical resistance or grain electrical resistance on the total electrical resistance. From Fig.6 and Fig.7, it can be concluded that the influence of grain

boundary conductivity on the total conductivity is more extraordinary than that of grain conductivity. This also infers that the ionic transmitted route is changed from grain conduction model into multi-channel grain boundary conduction model, which is preferred transport route. By contrasting with typical microstructure graph, the number of coarse grains and the distribution of that could control the grain impedance. The disadvantageous factor of more coarse grains on ionic conductivity at high temperature is involved in the limitation of grain electrical resistance. The effect of Mg ion on the grain boundary conductivity reveals that high-pure grain boundary is beneficial to total conductivity at high temperature. Although the grain boundary of Zr-Y-Mg-Al-Ca-O ceramic in this study is not high-pure, there is as a second-phase among grains, called partial clogged grain boundary, which will be transforming to good conductor with increase of temperature.

From the figure 7, the maximum ionic conductivity obtained in Zr-Y-Mg-Al-Ca-O ceramics is  $0.143 \text{ Scm}^{-1}$  at 1223K. The highest ionic conductivity obtained in this work is better than that of  $\text{Sm}_{2-x}\text{La}_x\text{Zr}_2\text{O}_7$  [14] and Sc-Yb-Zr-Ca-O at 1223K [15]. The complex doped electrolyte in this work showed an increased ionic conductivity which is also better than that of 8YSZ reported in literature [16] at the same temperature.

## 4. Conclusions

From the results, we found the densification rate at initial stage of sintering can improve the final sintering through the effect of covering PVA on the sintering mechanisms. The elements distribution, microstructure, phase assemblage, ionic conductivity and conduction mechanism of Zr-Y-Mg-Al-Ca-O ceramics were investigated. The main conclusions are summarized as:

(1) The doping elements are uniformly distributed in the Zr-Y-Mg-Al-Ca-O ceramics. The prepared Zr-Y-Mg-Al-Ca-O ceramics have a polymorph structure which could gradually evolve with increasing of temperature.

(2) With increase of Y/Mg ion ratio, the ionic conductivity sequence of prepared samples is S3>S2>S1 at high temperature. The maximum ionic conductivity at 1223K in this work reaches to  $0.143 \text{ Scm}^{-1}$  which is better than that of  $\text{Sm}_{2-x}\text{La}_x\text{Zr}_2\text{O}_7$  and Sc-Yb-Zr-Ca-O at 1223K, even better than that of 8YSZ at the same temperature.

(3) The influence of grain boundary conductivity on the total conductivity is more extraordinary than that of grain conductivity which related to the distribution of ion and the distributed ion category along grain boundary.

## Declarations

### Acknowledgments

The authors are grateful for the Analysis and Testing Center of Huazhong University of Science and Technology for XRD and SEM tests, as well as Ningbo Institute of Industrial Technology for ionic conductivity tests. The authors also thank Dr. Qingqing Yang and Dr. Huatang Tan for particle size testing.

## References

- [1] D. Maeland, C. Suci, I. Waernhus, A.C. Hoffmann. *J. Eur. Ceram. Soc.* 29 (2009) 2537–2547.
- [2] S. Tekeli. *Mater. Des.* 28 (2007) 713–716.
- [3] T. Jardiel, B. Levenfeld, R. Jimenez, A. Varez. *Ceram. Int.* 35 (2009) 2329–2335.
- [4] T. Zhang, Z. Zeng, H. Huang, P. Hing, J. Kinler. *Mater. Lett.* 57 (2002) 124–129.
- [5] F.L. Lowrie, R.D. Rawlings. *J. Eur. Ceram. Soc.* 20 (2000) 751–760.
- [6] J. Patakangas, Y. Ma, Y. Jing, P. Lund. *J. Power Sources* 263 (2014) 315-331.
- [7] J. Yang, B.F. Ji, J.Y. Si, Q.Z. Zhang, Q.Y. Yin, J.S. Xie, C.A. Tian. *Int. J. Hydrogen Energy* 41 (2016) 15979-15984.
- [8] K. Sugihara, M. Asamoto, Y. Itagaki, T. Takemasa, S. Yamaguchi, Y. Sadaoka, H. Yahiro. *Solid State Ionics* 262 (2014) 433-437.
- [9] T. Sato, M. Ishitsuka, M. Shimada. *Mater. Des.* 9 (1998) 204-212.

- [10] M.V. Swain, R.C. Garvie, R.H.J. Hannink. J. Am. Ceram. Soc. 66 (1983) 358-362.
- [11] H. Tsubakino, K. Sonoda, R. Nozato. J. Mater. Sci. Lett. 12 (1993) 196-198.
- [12] S. Tekeli. Mater. Des. 28 (2007) 713–716.
- [13] Y.G.Hu, J.Z. Xiao, F. Xia, H.B. Zhang. J. Wuhan Uni. Tech.-Mater. Sci. Ed. 28 (2013) 483-486.
- [14] Z.G. Liu, J.H. Ouyang, Y. Zhou, J. Xiang, X.M. Liu, Mater. Des. 32 (2011) 4201–4206.
- [15] Z.G. Lv, R.S. Guo, P. Yao, F.Y. Dai, Mater. Des. 28 (2007) 1399–1403.
- [16] C.S. Hellberg, N. Bernstein, S.C. Erwin. APS Meeting. (2016).

## Figures

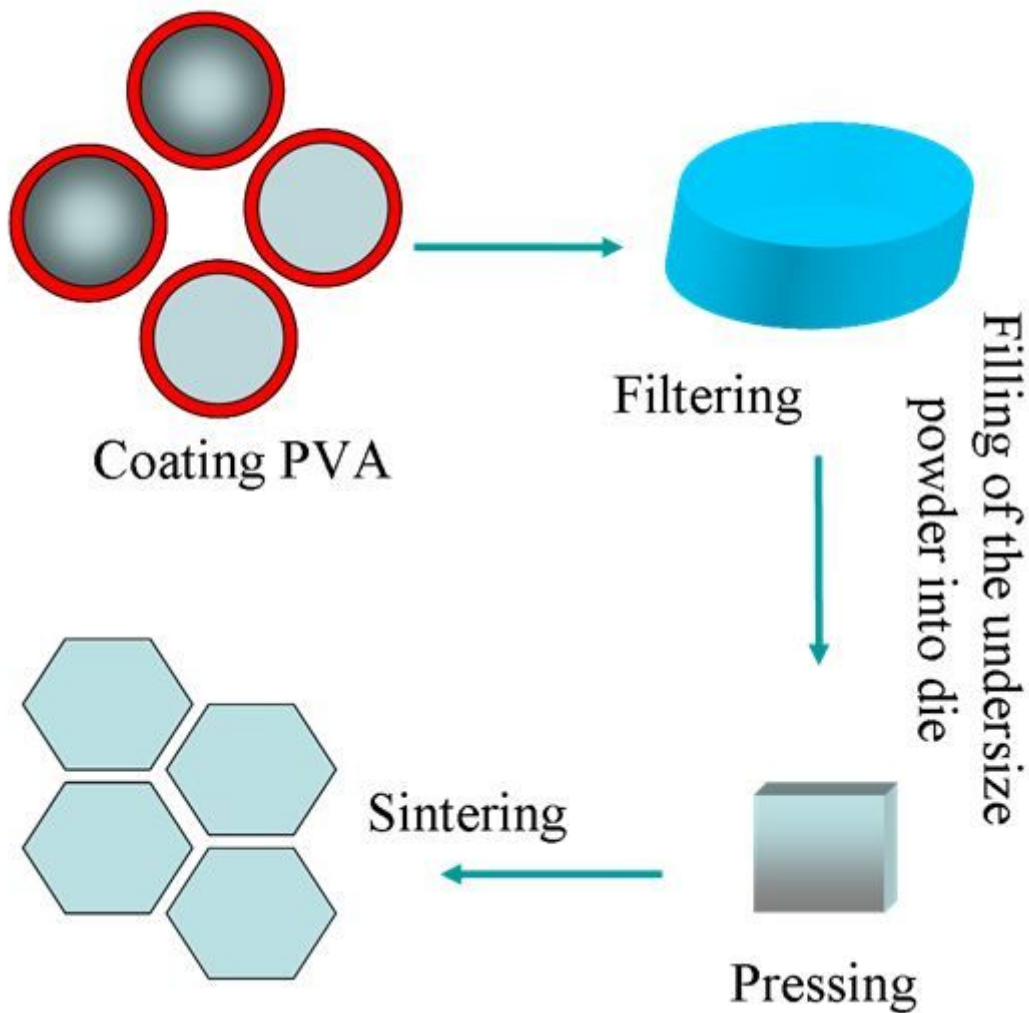
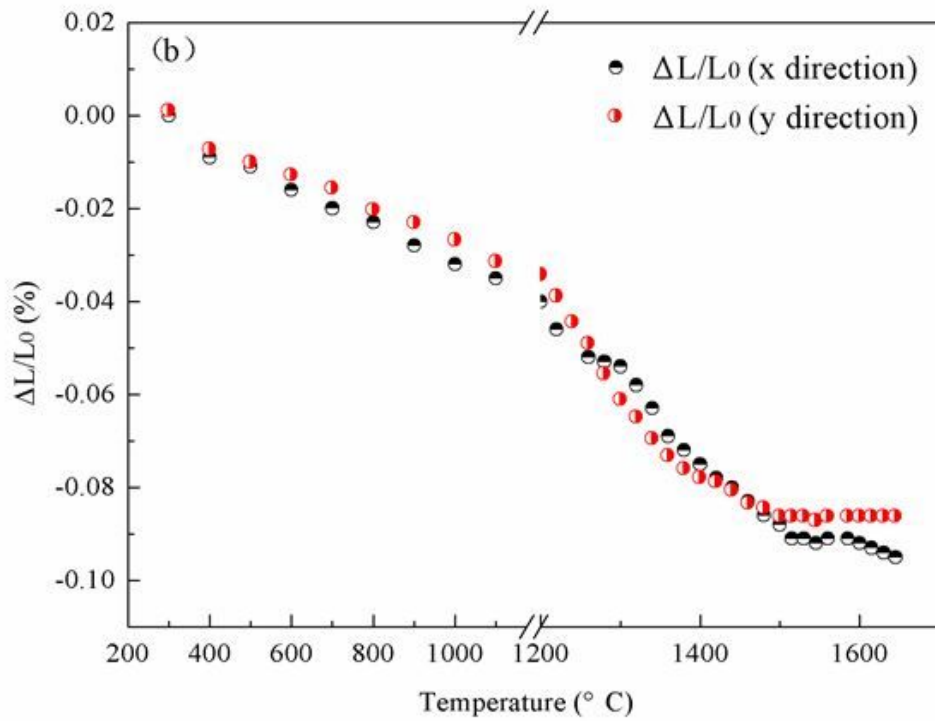
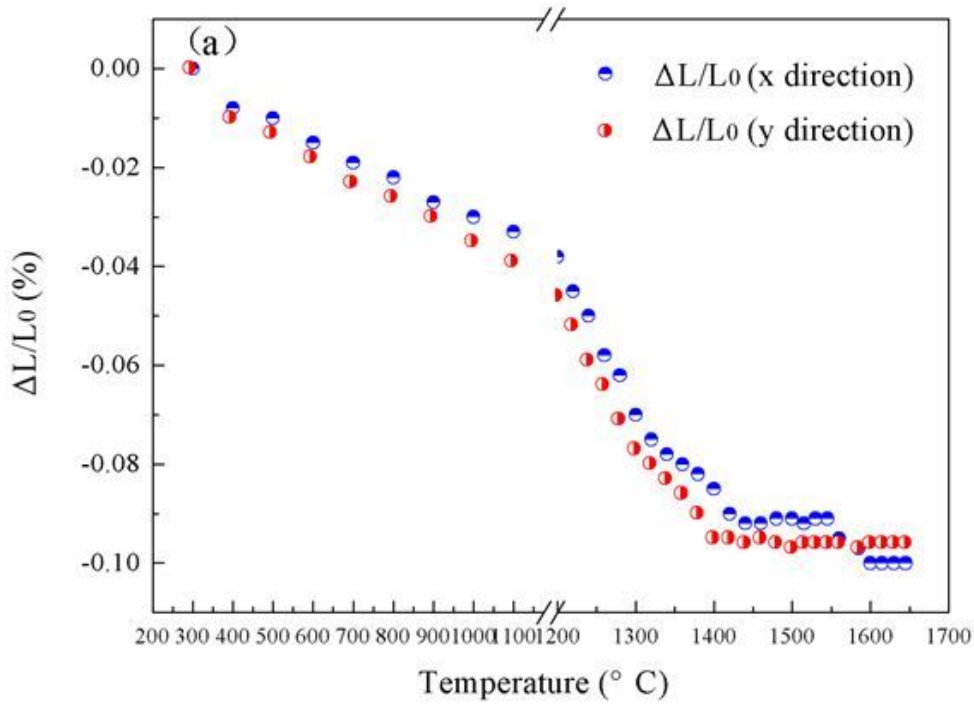


Figure 1

The preparation chart of ZrO<sub>2</sub> electrolytes.



**Figure 2**

The main sintering curve of SP1 (a) and SP2 (b).

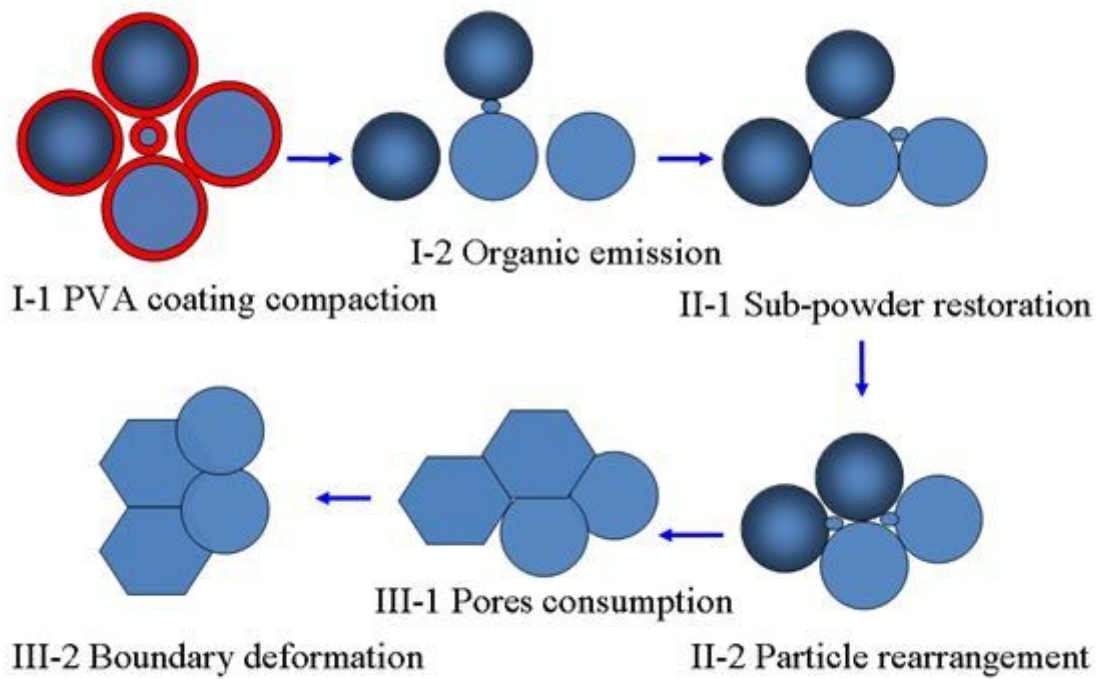


**Figure 3**

The schematic representation of the six sintering stages of polycrystalline zirconia

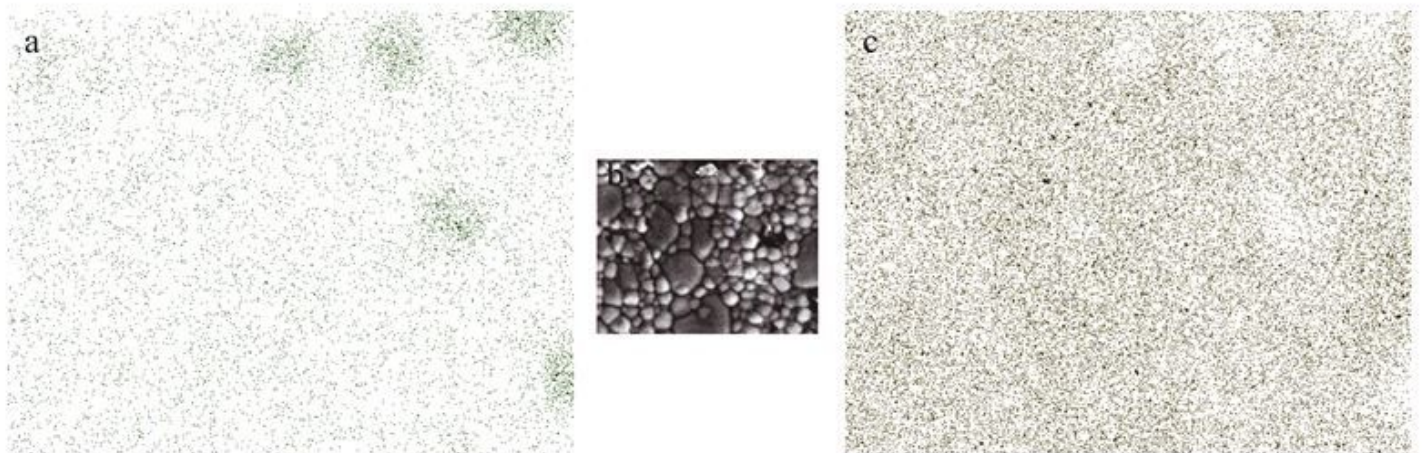


**Figure 4**

Element distribution maps of Mg (a) and Y (c) obtained by the sintered PSZ sample (b).

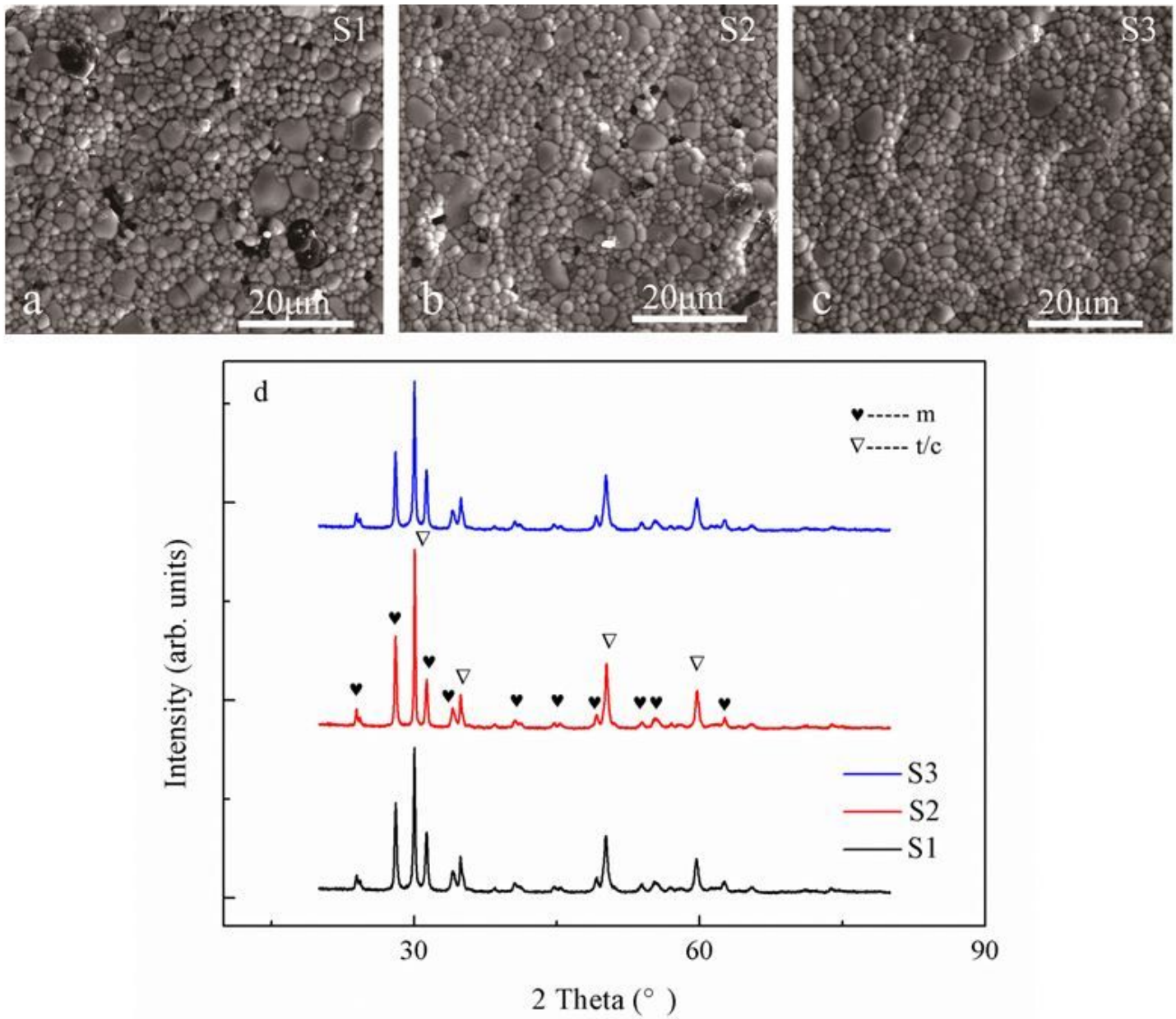


**Figure 5**

The heterogeneous microstructure and coarse grains (SEM) and phase composition (XRD) obtained by the sintered PSZ sample.

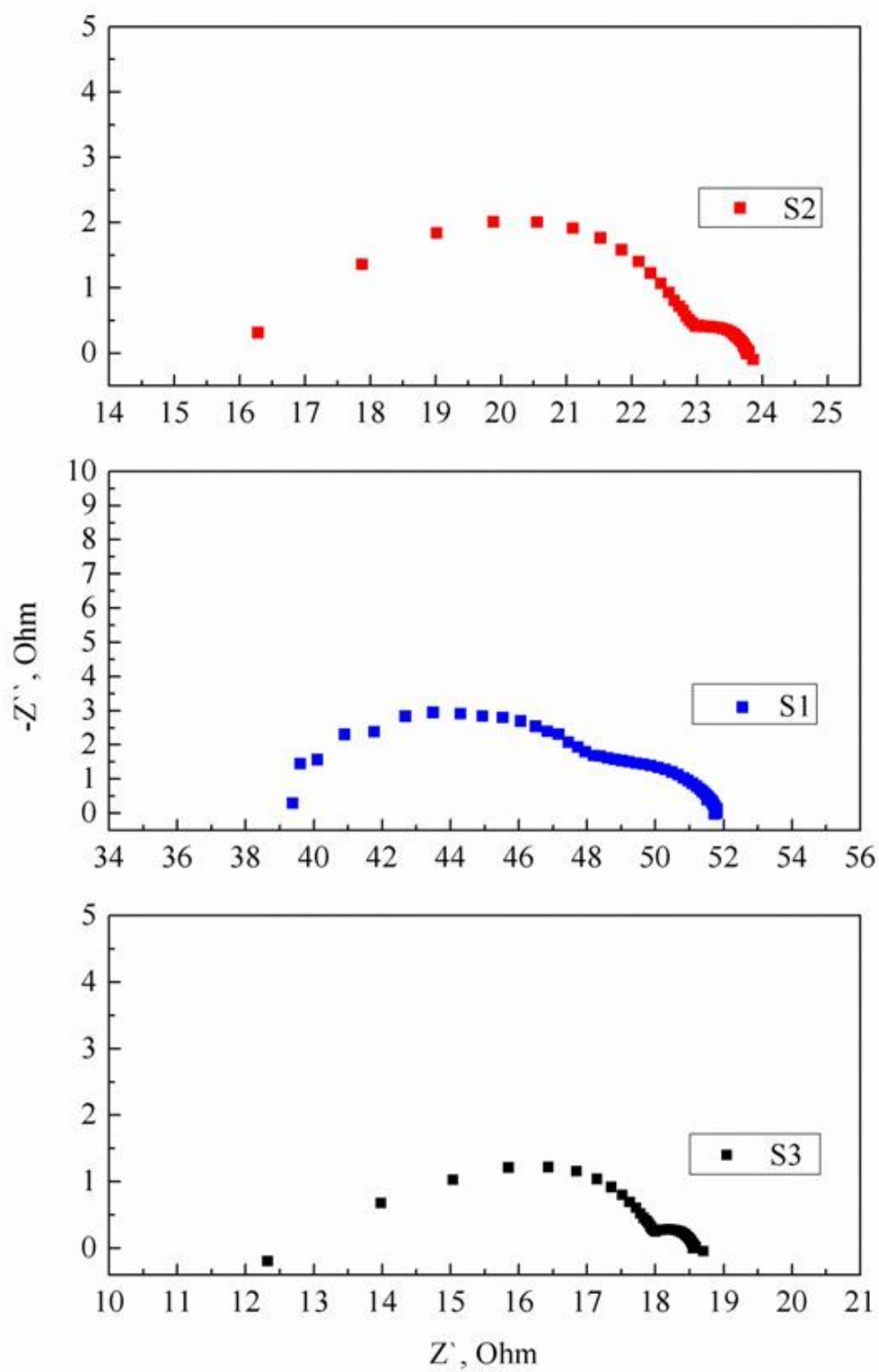


**Figure 6**

Impedance spectra tested at 1223K of Zr-Y-Mg-Al-Ca-O ceramics varied with the Y/Mg ion rate.

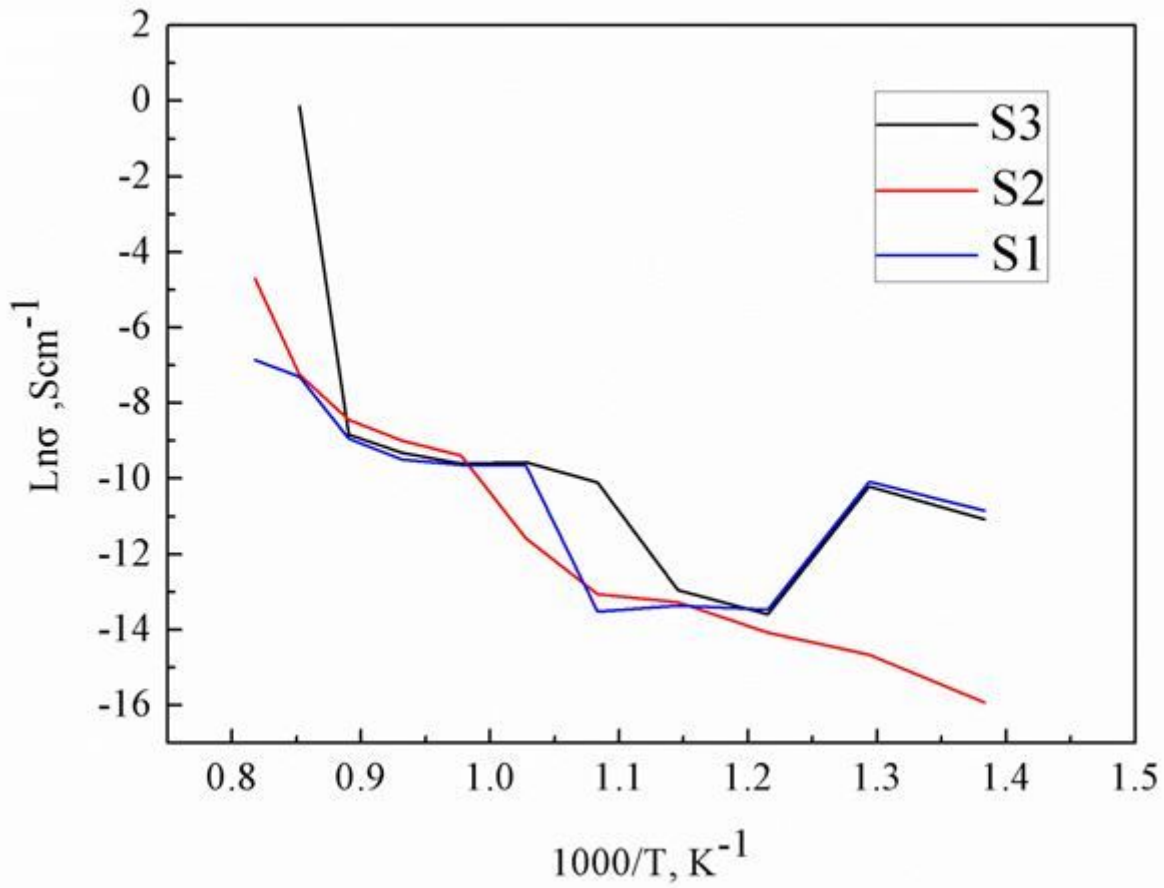


**Figure 7**

Arrhenius plots of conductivity of Zr-Y-Mg-Al-Ca-O ceramics varied with the Y/Mg ion rate over wide temperature window (723-1273K).